# Determining Thermophysical Properties of Normal and Metastable Liquid Zr-Fe Alloys by Electrostatic Levitation Method

C.H. ZHENG, H.P. WANG, P.F. ZOU, L. HU, and B. WEI

The thermophysical properties of liquid Zr-Fe alloys were experimentally measured by an electrostatic levitation technique. A series of undercoolings from 45 K to 410 K were achieved for these liquid alloys in the natural radiation cooling process. Since the experiments were conducted in high-vacuum and containerless conditions, the ratio of the specific heat to the hemispherical emissivity was deduced and showed a quadratic relationship with temperature. For the eutectic $Zr_{76}Fe_{24}$ alloy, the hypercooling of 306 K and hemispherical emissivity were derived theoretically due to its low liquidus temperature and scarce volatilization. Through digital image processing, the alloy densities were measured, and the results depended linearly on temperature over a wide temperature range covering both superheated and undercooled liquid states. The absolute value of the temperature coefficient tended to increase with increasing Fe contents, indicating that the liquid density sensitivity increased with increasing Fe contents. The surface tension and viscosity were also determined by a drop oscillation method under the electrostatic levitation condition.

https://doi.org/10.1007/s11661-020-05820-2


## I. INTRODUCTION

DATA on the thermophysical properties of liquid alloys are required for both fundamental research and engineering applications.[1–5] For instance, the density of a liquid alloy is one of the fundamental properties as it is an essential parameter used for the determination of other features, including thermal expansion, excess volume, specific heat, surface tension, viscosity, *etc*.[6,7] In addition, studies on density are conducive to understanding macro phase transitions such as liquid–liquid, liquid–solid and even glass transitions. Data on these properties also contribute to further understanding the liquid structure at the atomic scale. In thermodynamic studies, such as CALPHAD and nucleation theories, an accurate specific heat is a necessary parameter.[8–10] The surface tension and viscosity characterize the kinetic features of liquid alloys, which are quite essential for the investigation of surface phenomena and inset convection heat transfer.[11,12] Furthermore, the thermophysical properties of undercooled alloys also play important roles in controlling the solidification process and exploring unknown metastable phases.

However, due to the high temperature and reactivity of liquid alloys, high-quality thermophysical data available for liquid alloys are scarce in the literature, especially for undercooled melts, where heterogeneous nucleation needs to be suppressed.[13–17] These problems are unavoidable in conventional measurements. Therefore, containerless methods, such as acoustic levitation, electromagnetic levitation (EML), and electrostatic levitation (ESL), are valid choices for determining the thermophysical properties of high-temperature liquid alloys.[18–23] Moreover, containerless conditions suppress heterogeneous nucleation and make the high undercooling of liquid alloys possible. In this way, the thermophysical properties of a liquid alloy in the high-temperature region can be determined. In comparison with other levitation methods, the ESL method has many merits due to the no stirring effect, the separation of heating and levitation, the spacious field of observation and so on. These advantages make the electrostatic levitation technique an ideal approach for determining the thermophysical properties of liquid alloys, in both superheated and undercooled states.

The Zr-Fe binary system has been utilized for a wide range of engineering applications.[24–26] Zr-rich Zr-Fe alloys have aroused great research interest in the nuclear industry due to their excellent mechanical properties, low neutron absorption cross section and good

C.H. ZHENG, H.P. WANG, P.F. ZOU, L. HU, and B. WEI are with the School of Physical Science and Technology, Northwestern Polytechnical University, Xi'an 710072, P.R. China. Contact e-mail: hpwang@nwpu.edu.cn
Manuscript submitted December 25, 2019.
Article published online May 23, 2020

corrosion resistance for high-temperature water. Therefore, many researchers focus on studying the corrosion resistance of Zr-based alloys.[27] In addition to the corrosion of the water and oxygen, hydrogen pickup is also a critical problem. Many researchers try their best to deal with this problem. Couet *et al.*[28] proposed that the oxide resistivity is proportional to the hydrogen pickup, which is greatly helpful to the understanding of the hydrogen pickup mechanism. Moreover, for the safety of nuclear reactors, an accurate safety assessment test is indispensable. These all require precise thermophysical properties of Zr-Fe alloys, especially in the liquid state. On the other hand, systematic thermophysical research on Fe-rich Zr-Fe alloys facilitates their commercial applications in modern composite steel.[10,29] In addition, Zr-Fe binary systems are an important branch of amorphous alloys. Metallic Zr-Fe glass has some unusual electrical and magnetic properties.[26,30] While the sizes of amorphous alloys limit their application, researchers wish to improve the glass-forming ability and obtain materials with better properties by designing the compositions of the alloys. Additionally, support is needed from the accurate thermophysical property data of alloys in metastable liquid states.

Although there are a few reports about the thermophysical properties of liquid Zr-Fe alloys, two major problems have led to a continued lack of systematic research on the physical properties of this alloy system.[31–33] One problem is the levitation difficulties, which occur because of the strong volatilization and magnetism of liquid Zr-Fe alloys. The other is the complexity of the Zr-Fe alloy system, which contains abundant liquid–solid/solid–solid reactions and a broad liquidus temperature range. Due to the abovementioned reasons, this work aims to explore the thermophysical properties, including the density, ratios between the specific heat and emissivity, surface tension, and viscosity of liquid Zr-Fe alloys in an extensive temperature range covering both the superheated and undercooled regimes by ESL. Correspondingly, the relationship between these properties with temperature and composition is summarized.

## II. METHODS

### A. *Sample Preparation*

The Zr-Fe alloy compositions chosen (10 pct Fe, 20 pct Fe, 24 pct Fe, 30 pct Fe, 40 pct Fe, 50 pct Fe, 84 pct Fe, 90.2 pct Fe) for experiments are illustrated in the Zr-Fe binary phase diagram[34] as shown in Figure 1. The Zr-Fe master alloys used for the experiments are prepared from 99.99 pct pure Fe and 99.95 pct pure Zr by arc melting in an Ar atmosphere. Then, the master alloys are divided into small portions and remelted by a laser under an Ar atmosphere. The size of samples is different for different measurements. For the density measurements, sample is weighted about 30 mg with a diameter approximately 2 mm in sphere, in order to restrain the oscillation and the deformation. For the surface tension and viscosity measurements,

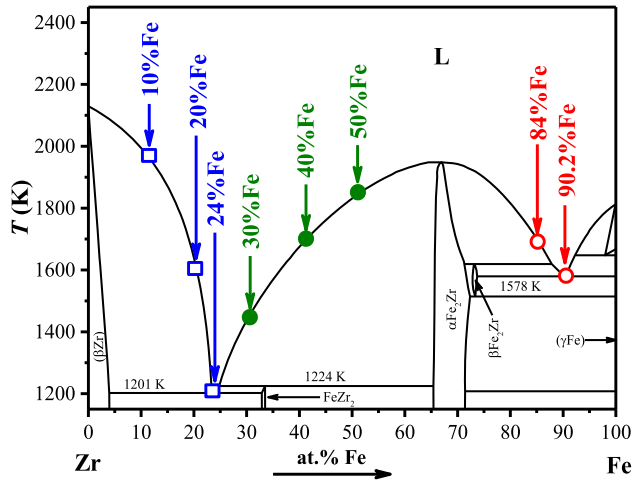


Fig. 1—The selected alloy compositions shown in the Zr-Fe binary phase diagram.

approximately 60 mg of the sample with a diameter of 2.5 mm is weighed, for the purpose of exciting oscillations easily.

### B. *Density Measurement*

The density, surface tension and viscosity of the Zr-Fe alloys are all measured by an ESL facility, and more details about the facility are described in the Reference [35]. A continuous wave SPI SP300 fiber laser with a wavelength of 1070 nm is used to heat the samples. The heating laser is started with a low power of approximately 20 W to preheat the sample before levitation. The sample is levitated between two vertical electrodes coupled with four side electrodes in a chamber evacuated to $1.0 \times 10^{-5}$ Pa. When levitation is steady, the sample is heated to be melted, generally with a melting plateau at the liquidus temperature shown on the temperature curve. As it is maintained in a containerless state, the melting sample tends to form a spherical shape because of the surface tension and surface charge distribution. When the sample is heated up to a superheated state, the laser is turned off, and the sample is purely cooled by natural radiation. The temperature of the samples is recorded by a commercial 2-color Metis M322 pyrometer manufactured by Sensortherm GmbH with a temperature range of 600 K to 2300 K. The parameters of the pyrometer are calibrated at the liquidus temperature $T_L$, and the parameters would be maintained in the whole process until the end of levitation. The images of the sample are recorded by a CMOS camera with a frequency of 90 to 120 Hz under UV background light during the entire cooling process. Then, the images are digitalized, and the volume of the sample is extracted. More details of the image processing process can be viewed in the Reference [36]. Considering the mass of the sample measured before and after the experiment, the density of liquid alloys can be obtained from the relationship $\rho = m/V$, where $m$ is the mass of the sample, and $V$ is the volume.

### C. *The Ratio of the Specific Heat to Emissivity*

During the density determination, the ratio of the specific heat to emissivity is measured at the same time by using natural radiation. The stable levitated sample is heated up to a superheated state, the heating laser is then shut down, and the sample is cooled by natural radiation. Since the electrostatic levitation system chamber is evacuated to $1.0 \times 10^{-5}$ Pa, the levitated drop would experience a pure natural radiative cooling period, and the heat balance equation can be expressed as follows[37]:

$$mC_{PL}R_c = \sigma_B AM\varepsilon_T\left(T^4 - T_r^4\right), \quad [1]$$

where $m$ is the mass of the sample, $C_{PL}$ is the constant pressure specific heat of the sample, $R_c$ is the cooling rate, which equates to $-\,\mathrm{d}T/\mathrm{d}t$, $\sigma_B$ is the Stefan–Boltzmann constant ($5.6703 \times 10^{-8}$ W m$^{-2}$ K$^{-4}$), $A$ is the surface area of the sample, $M$ is the molar mass, $\varepsilon_T$ is the hemispherical total emissivity, $T$ is the temperature of the sample, and $T_r$ is the environment temperature. The surface area can be obtained through image processing, and the cooling rate can be derived from the cooling temperature curve. Therefore, this expression can be rewritten as follows[38]:

$$\xi_T = \frac{C_{PL}}{\varepsilon_T} = \frac{M\sigma_B A\left(T^4 - T_r^4\right)}{mR_c}. \quad [2]$$

Then, the ratio of the specific heat to emissivity $\xi_T$ can be derived, since all the parameters on the right side can be obtained. Through the ratio $\xi_T$, the material radiation dissipation capability can be described. In addition, from Eq. [2], the total hemispherical emissivity can be derived if the constant pressure specific heat is known, and *vice versa*.

### D. *Surface Tension and Viscosity*

The surface tension and viscosity of the sample are measured by the drop oscillation method under electrostatic levitation conditions with the vacuum evacuated to $1.0 \times 10^{-5}$ Pa. When the sample is levitated steadily in the electrostatic field, the temperature of the liquid sample is maintained at the preset value by controlling the laser output. After ensuring both the position and temperature of the sample are stable, a sinusoidal AC voltage of 900 mV is superimposed on the high voltage amplitude, which is connected to the top electrode. Then, the droplet is excited to oscillate in an axisymmetric oscillation mode. When an isolated liquid drop undergoes an axisymmetric oscillation with a small amplitude, the characteristic oscillation frequency of the drop corresponding to the $n$th order mode can be described as follows[39]:

$$(2\pi\omega_n)^2 = n(n-1)(n+2)\frac{\sigma}{\rho r_0^3}, \quad [3]$$

where $\omega_n$ is the oscillation frequency at the $n$th order mode, $r_0$ is the radius of the droplet with a spherical shape, $\sigma$ and $\rho$ are the density and surface tension, respectively, of the liquid alloy. For the axisymmetric oscillating isolated droplet, $n$ is 2, and the characteristic frequency could be expressed by the following equation:

$$\omega_2^2 = \frac{2\sigma}{\pi^2\rho r_0^3}, \quad [4]$$

where $\omega_2$ is the characteristic frequency for $n = 2$. The frequency of the oscillating droplet can be determined through the variation of the droplet oscillating amplitude, which is recorded by oscillation amplitude detection. The droplet is projected on the electrophotonic detector through the collimated laser beam to detect the position. To improve the accuracy of detecting the oscillation amplitude, the projection is masked by a grating with a narrow slit. There is also a narrow band interference filter at the laser wavelength that is put in front of the electrophotonic detector to filter stray light. The oscillation of the sample drop can be observed directly from the image captured by a CMOS camera. As shown in Figure 2(a), there is a typical second-order axisymmetric oscillation process that occurs during excitation. Since the temperature of the sample is changed, the frequency of the excitation voltage signal is adjusted to make the sample oscillate by a second-order axisymmetric mode. After the excitation is turned off, a transient free attenuation in the oscillation occurs, and the decay curve can be detected in this period, as shown in Figure 2(b). Correspondingly, the characteristic frequency can also be analyzed from the decay curve by the Fast Fourier Transform (FFT), as shown in Figure 2(c). Then, the surface tension can be derived from Eq. [4] by performing the axisymmetric second-order oscillation approximation of an isolated droplet. Apparently, the effect of the electric field and gravity should be considered. The frequency terms used to correct the axisymmetric second-order-mode, which were modified by Feng and Beard,[40] are expressed as follows:

$$\omega_{2m}^2 = \omega_2^2\left(1 - \frac{Q_s^2}{64\pi^2 r_0^3\sigma\varepsilon_0}\right)[1 - F(\sigma, q, e)], \quad [5]$$

$$F(\sigma, q, e) = \frac{\left(243.31\sigma^2 - 63.14q^2\sigma + 1.54q^4\right)e^2}{176\sigma^3 - 120q^2\sigma^2 + 27q^2\sigma - 2q^6} \quad [6]$$

$$e = E^2 r_0\varepsilon_0, \quad [7]$$

$$q^2 = \frac{Q_s^2}{16\pi^2 r_0^2\varepsilon_0}, \quad [8]$$

$$\frac{U}{L}Q_s = mg, \quad [9]$$

where $\omega_{2m}$ is the measured frequency, $E$ is the applied electric field, which can be derived from $E = U/L$ by the voltage $U$ and distance $L$ between the vertical electrodes, and $Q_s$ is the charge of the drop, whcih can be

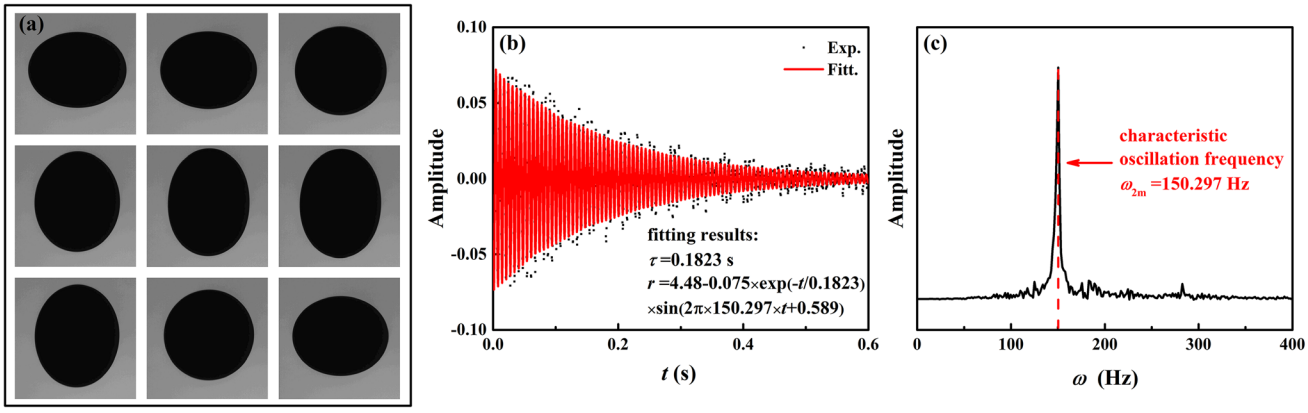


Fig. 2—The measurement of the surface tension and viscosity by the oscillation method coupled with ESL: (*a*) a period of second-order axisymmetric oscillation recorded by a CMOS camera; (*b*) a typical decay curve detected after turning off the excitation signal; (*c*) the characteristic oscillation frequency.

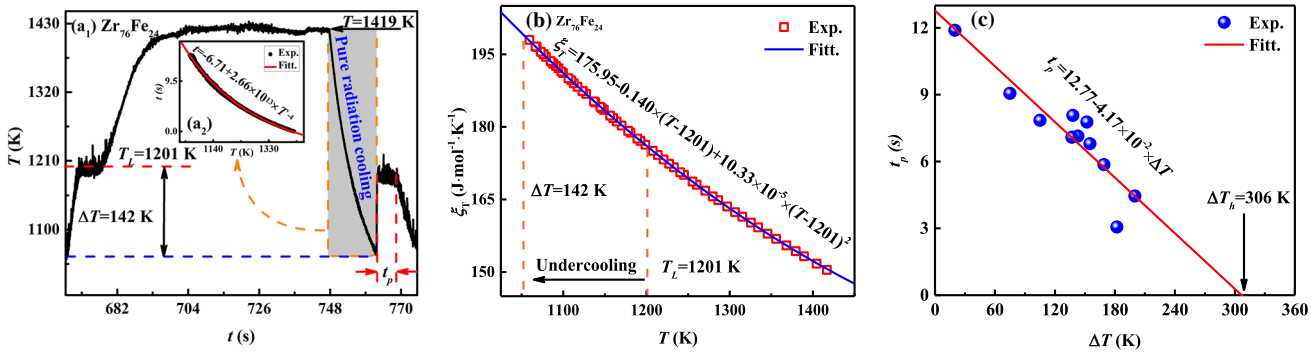


Fig. 3—The thermal characteristics of the electrostatically levitated Zr-Fe alloys: ($a_1$) the temperature curve of the $Zr_{76}Fe_{24}$ alloy; ($a_2$) the period of pure radiation cooling; (*b*) the ratio of the specific heat to emissivity (*c*) the solidification platform time $t_p$ after recalescence *vs* the undercooling $\Delta T$.

determined by Eq. [9]. Combining Eqs. [4] to [9], the corrected surface tension is obtained.

Meanwhile, through the same oscillation signal, another important thermophysical property viscosity $\eta$ of the droplet is given[41]:

$$\eta = \frac{\rho r_0^2}{5\tau}, \qquad [10]$$

where $\tau$ is the decay time, which can be derived from the transient free oscillation signal, as shown in Figure 2(b).

## III. RESULTS AND DISCUSSION

### A. *The Ratio of the Specific Heat to Emissivity*

During the experiments, most of the samples are superheated 100 K to 300 K above the liquidus temperature, and then cooled down by pure radiation.

As shown in Figure 3(a1), when the $Zr_{76}Fe_{24}$ droplet is heated to 1419 K, which is 218 K above the liquidus temperature of 1201 K, the heating laser is shut down. Then, the melt is cooled down only by natural radiation. With the decrease in the temperature, the liquid alloy reaches a metastable undercooling state. Then, the recalescence phenomenon, a sudden 129 K temperature increase caused by the latent heat owing to the eutectic reaction, appears at the undercooling of 142 K.

Thanks to the high vacuum and containerless environment, the liquid Zr-Fe alloys experience pure radiation cooling. In addition, the ratio of the specific heat to emissivity $\xi_T$ can be derived by Eq. [2] from the shadow range shown in Figure 3(a1). The surface area $A$ can be derived from the digital images. The cooling rate $R_c$ can be derived from the relationship between time $t$ and temperature $T$, which can be expressed as follows:

$$t = a + bT^{-4}, \qquad [11]$$

where $t$ is time. The fitting results are shown both in Figure 3(a2) and Table I. As shown in Figure 3(b), the results of $\xi_T$ can be fitted by a quadratic equation of temperature as follows:

$$\xi_T = \xi_0 + C_1(T - T_L) + C_2(T - T_L)^2, \qquad [12]$$

where $\xi_0$ presents the ratio at the liquidus temperature, $C_1$ and $C_2$ are constants. The fitting results and measurement uncertainty are all listed in Table I. It

**Table I. The Measured Ratio of the Specific Heat to Emissivity for the Liquid Zr-Fe Alloys**

| Alloy | $T_L$ (K) | Parameters of Cooling Curves | | | $C_{PL}/\varepsilon_L$ Ratio | | | Temperature Range (K) | Undercooling (K) | Uncertainty of $C_{PL}/\varepsilon_L$ (Pct) |
|---|---|---|---|---|---|---|---|---|---|---|
| | | $a$ (s) | $b$ ($10^{13}$ s K$^4$) | $R_c$ (at $T_L$) (K s$^{-1}$) | $\xi_0$ (J mol$^{-1}$ K$^{-1}$) | $C_1$ (J mol$^{-1}$ K$^{-2}$) | $C_2$ ($10^{-5}$ J mol$^{-1}$ K$^{-3}$) | | | |
| $Zr_{90}Fe_{10}$ | 1998 | − 1.95 | 3.45 | 230.73 | 152.40 | − 0.070 | 4.94 | 1588 to 2058 | 410 | ± 2.11 |
| $Zr_{80}Fe_{20}$ | 1649 | − 2.95 | 3.82 | 79.80 | 193.68 | − 0.112 | 8.41 | 1259 to 1890 | 390 | ± 2.11 |
| $Zr_{76}Fe_{24}$ | 1201 | − 6.71 | 2.66 | 23.48 | 175.95 | − 0.140 | 10.33 | 1059 to 1419 | 142 | ± 2.11 |
| $Zr_{70}Fe_{30}$ | 1487 | − 2.83 | 2.78 | 65.38 | 143.75 | − 0.092 | 7.65 | 1109 to 1727 | 378 | ± 2.11 |
| $Zr_{60}Fe_{40}$ | 1652 | − 3.25 | 3.50 | 87.89 | 153.69 | − 0.088 | 6.23 | 1332 to 1817 | 320 | ± 2.11 |
| $Zr_{50}Fe_{50}$ | 1830 | − 2.82 | 3.63 | 141.35 | 145.36 | − 0.073 | 4.73 | 1564 to 1830 | 266 | ± 2.14 |
| $Zr_{16}Fe_{84}$ | 1730 | − 7.81 | 7.75 | 49.99 | 240.84 | − 0.117 | 10.46 | 1578 to 1789 | 152 | ± 2.12 |
| $Zr_{9.8}Fe_{90.2}$ | 1578 | − 7.28 | 5.27 | 46.42 | 181.29 | − 0.103 | 5.66 | 1533 to 1643 | 45 | ± 2.11 |

can be seen that $Zr_{16}Fe_{84}$ alloy has the largest value of $\xi_0$, 240.84 J mol$^{-1}$ K$^{-1}$, which means the undercooled liquid $Zr_{16}Fe_{84}$ alloy has the weakest radiation dissipation capability. The results that the liquid $Zr_{16}Fe_{84}$ alloy has the second lowest cooling rate at liquidus temperature of 1730 K also substantially confirm this view.

As shown in Figure 3(a1), after recalescence, there is a solidification plateau with a width $t_p$. Since Figure 3(c) shows the relationship between $t_p$ and $\Delta T$, and the hypercooling $\Delta T_h$ of 306 K is obtained by extending the fitting curve at $t_p = 0$. Furthermore, due to the extremely short time of recalescence, the heat emitted during recalescence is negligible. Then the temperature-averaged constant pressure specific heat $C_{PL,av}$ of the undercooled liquid $Zr_{76}Fe_{24}$ alloy can be derived by[37]:

$$C_{PL,av} = \frac{\Delta H_f}{\Delta T_h}, \qquad [13]$$

where $\Delta H_f$ is the specific enthalpy of fusion. For $Zr_{76}Fe_{24}$ alloy, the specific enthalpy of fusion $\Delta H_f$ determined by the differential scanning calorimeter (DSC) is 10454.11 J mol$^{-1}$. Then, the temperature-averaged constant pressure specific heat $C_{PL,av}$ of the undercooled liquid $Zr_{76}Fe_{24}$ alloy is 34.16 J mol$^{-1}$ K$^{-1}$. Moreover, by combining the specific heat and the ratio of the specific heat to emissivity listed in the Table I, the hemispherical total emissivity of the undercooled liquid $Zr_{76}Fe_{24}$ alloy can be approximated, and the results can be expressed as follows:

$$\varepsilon_{T,Zr_{76}Fe_{24}} = 0.194 + 1.53 \times 10^{-4}(T - 1201). \qquad [14]$$

According to Eq. [14], the hemispherical total emissivity of the liquid $Zr_{76}Fe_{24}$ alloy is approximated to be 0.194 at its liquidus temperature.

## B. *Density and Excess Volume*

Through the combination of the volume extracted from the digital images and the mass of the sample, the density of the alloy is derived. Based on the liquidus temperature change tendency and solidification phase composition, the experimental density results of the different compositions are divided into three regions. As shown in Figure 4(a), the liquid densities of $Zr_{90}Fe_{10}$, $Zr_{80}Fe_{20}$, and $Zr_{76}Fe_{24}$ alloys increase with increasing Fe contents. Additionally, the temperature range shifts to the low temperature due to the drop in the liquidus temperature. The liquid densities of $Zr_{70}Fe_{30}$, $Zr_{60}Fe_{40}$, and $Zr_{50}Fe_{50}$ alloys increase with increasing Fe contents, as shown in Figure 4(b), while the temperature range shifts to high temperatures due to the increase in the liquidus temperature. However, the liquid densities of $Zr_{16}Fe_{84}$ and $Zr_{9.8}Fe_{90.2}$ alloys decrease with increasing Fe contents, as shown in Figure 4(c). And the temperature range also shifts to low temperatures due to the drop in the liquidus temperature. Furthermore, it is clear that the liquid density decreases linearly with increasing temperature in both the superheated and undercooled states, which is consistent in different Zr-Fe

alloys. The linear relationships with temperature can be expressed as follows:

$$\rho = \rho_L + \frac{\partial \rho}{\partial T}(T - T_L), \qquad [15]$$

where $\rho_L$ is the density at the liquidius temperature $T_L$, and $\partial\rho/\partial T$ is the temperature coefficient. The experimental data are fitted with Eq. [15], and the detailed results are shown in Table II. A series of maximum undercooling are realized during the liquid density measurements for the $Zr_{100-x}Fe_x$ alloys with $x$ = 10, 20, 24, 30, 40, 50, 84, and 90.2 are 410 K, 390 K, 142 K, 378 K, 320 K, 266 K, 152 K, and 45 K, respectively. Although the largest undercooling is obtained in the liquid $Zr_{90}Fe_{10}$ alloy, the largest ratio between the undercooling and liquidus temperature is obtained by the liquid $Zr_{70}Fe_{30}$ alloy. It can be seen that the liquid densities of the $Zr_{100-x}Fe_x$ alloys with $x$ = 10, 20, 24, 30, 40, 50, 84, and 90.2 at the liquidus temperature are 6.35, 6.51, 6.69, 6.54, 6.69, 6.65, 7.22 and 7.24 g cm$^{-3}$, respectively. Besides, the temperature coefficients of the $Zr_{100-x}Fe_x$ alloys with $x$ = 10, 20, 24, 30, 40, 50, 84, and 90.2 are − 2.55, − 2.91, − 3.44, − 3.30, − 3.55, − 3.99, − 8.40 and − 6.51 with unit $10^{-4}$ g cm$^{-3}$ K$^{-1}$, respectively. It can be seen that the absolute value of the temperature coefficient tends to increase with increasing Fe contents, which reveals that the liquid density sensitivity to temperature is increasing with increasing Fe contents. There are few reports on the density of liquid Zr-Fe alloys. Compared with the values measured by Ohishi *et al.*,[33] the density value differences at the liquidus temperature for the $Zr_{76}Fe_{24}$ and $Zr_{50}Fe_{50}$ alloys are 1.5 and 0.49 pct, respectively.

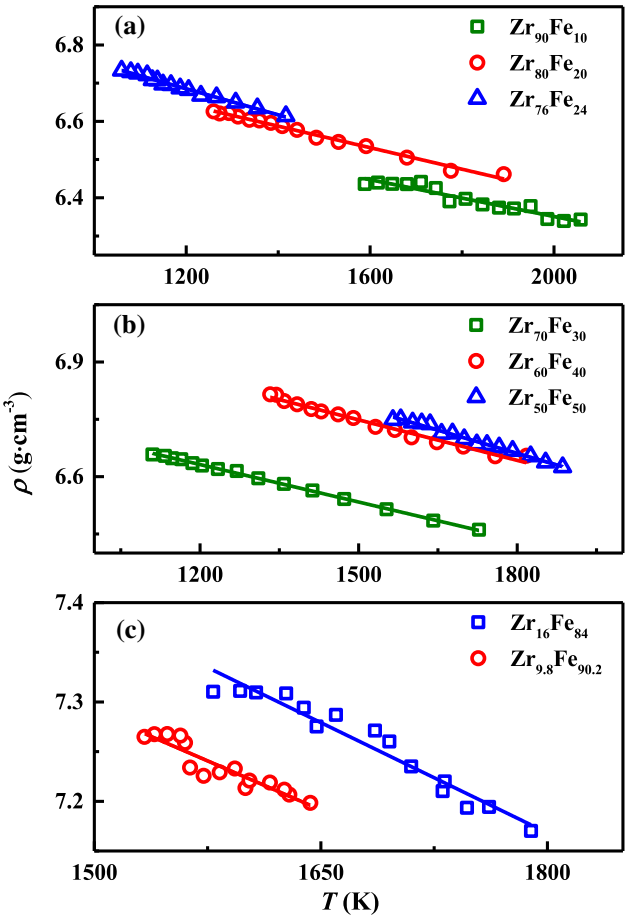


Fig. 4—The measured density values of liquid Zr-Fe alloys: (*a*) $Zr_{100-x}Fe_x$ ($x$ = 10, 20, 24); (*b*) $Zr_{100-x}Fe_x$ ($x$ = 30, 40, 50); (*c*) $Zr_{100-x}Fe_x$ ($x$ = 84, 90.2).

Because the liquidus temperature of each alloy is different, Figure 5(a) shows the density values change with varying the Fe content in the temperature range of 1500 K to 1900 K. The liquid densities of the pure substances Fe and Zr measured by Lee *et al.*[42] and Wang *et al.*[6] are compared together in Figure 5(a). Since the temperature range of measurements for each alloys not all cover 1500 K to 1900 K, the solid points are experimental results, and the hollow points are the data extrapolated from the experimental results. It can generally be seen that the liquid densities of the Zr-Fe alloys increase with increasing Fe contents at the same temperature, although there are two tiny drops near the two eutectic compositions $Zr_{76}Fe_{24}$ and $Zr_{9.8}Fe_{90.2}$. The liquid density of $Zr_{76}Fe_{24}$ alloy at 1500 K is 6.58 g cm$^{-3}$, which is 0.39 pct larger than that of $Zr_{80}Fe_{20}$ alloy and 0.74 pct larger than that of $Zr_{70}Fe_{30}$ alloy, while the liquid density of $Zr_{9.8}Fe_{90.2}$ alloy at 1500 K is 7.30 g cm$^{-3}$ which is 1.55 pct less than that of $Zr_{16}Fe_{84}$ alloy, and is 1.86 pct larger than the liquid density of Fe at 1500 K, as extrapolated from a reference.[42] The liquid density at 1900 K of $Zr_{76}Fe_{24}$

**Table II. The Measured Density of the Liquid Zr-Fe Alloys**

| Alloy | $T_L$ (K) | Temperature range (K) | Undercooling $\Delta T$(K) | $\Delta T/T_L$ | $\rho_L$(g cm$^{-3}$) | $\partial\rho/\partial T$ ($10^{-4}$ g cm$^{-3}$ K$^{-1}$) | Uncertainty (at $T_L$) |
|---|---|---|---|---|---|---|---|
| $Zr_{90}Fe_{10}$ | 1998 | 1588 to 2058 | 410 | 0.205 | 6.35 | − 2.55 | ± 7.51 pct |
| $Zr_{80}Fe_{20}$ | 1649 | 1259 to 1890 | 390 | 0.236 | 6.51 | − 2.91 | ± 0.72 pct |
| $Zr_{76}Fe_{24}$ | 1201 | 1059 to 1419 | 142 | 0.118 | 6.69 | − 3.44 | ± 0.67 pct |
| $Zr_{70}Fe_{30}$ | 1487 | 1109 to 1727 | 378 | 0.254 | 6.54 | − 3.30 | ± 0.70 pct |
| $Zr_{60}Fe_{40}$ | 1652 | 1332 to 1817 | 320 | 0.193 | 6.69 | − 3.55 | ± 0.68 pct |
| $Zr_{50}Fe_{50}$ | 1830 | 1564 to 1830 | 266 | 0.145 | 6.65 | − 3.99 | ± 0.78 pct |
| $Zr_{16}Fe_{84}$ | 1730 | 1578 to 1789 | 152 | 0.087 | 7.22 | − 8.40 | ± 0.81 pct |
| $Zr_{9.8}Fe_{90.2}$ | 1578 | 1533 to 1643 | 45 | 0.028 | 7.24 | − 6.51 | ± 1.08 pct |

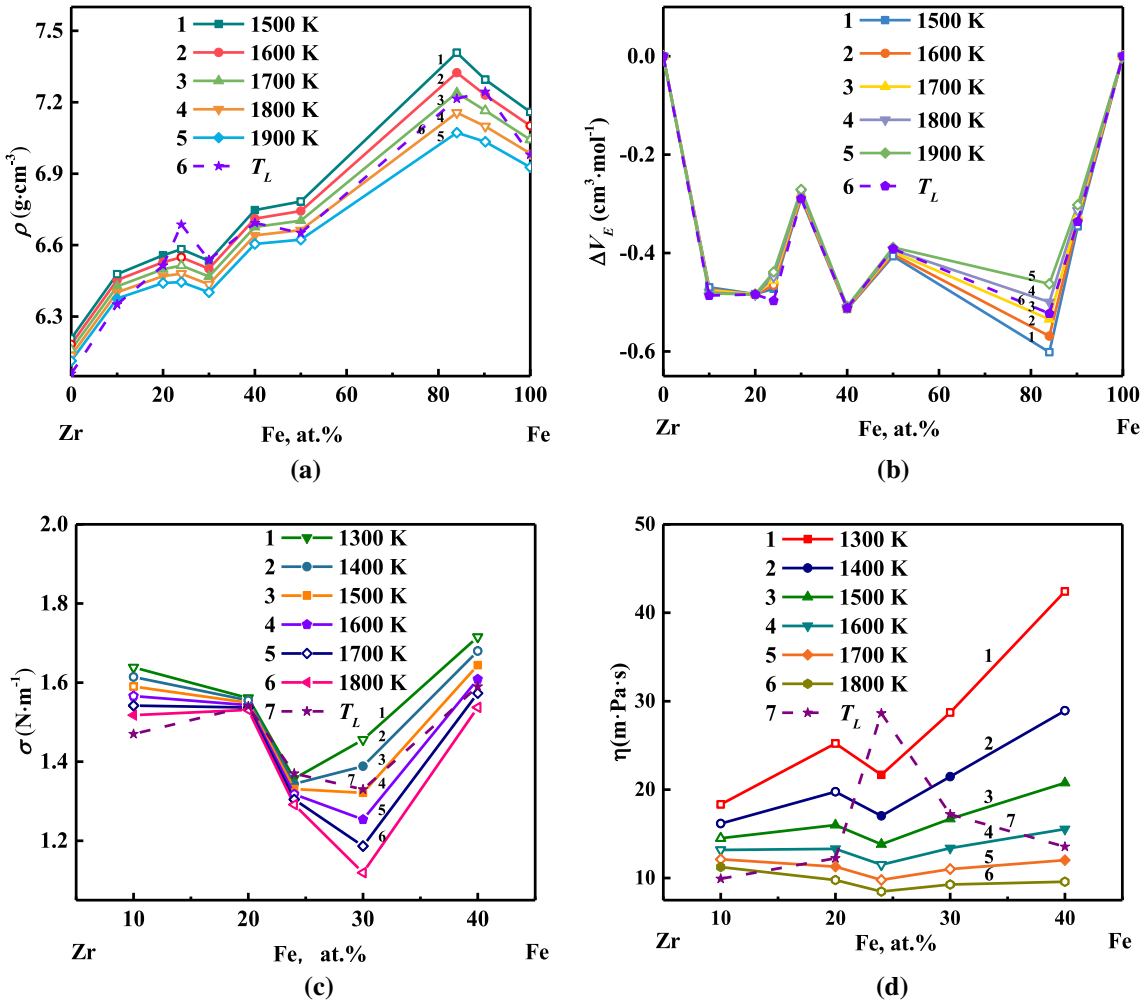


Fig. 5—The density and excess volume of the liquid Zr-Fe alloys: (*a*) the liquid density *vs* the Fe content; (*b*) the excess volume *vs* the Fe content; (*c*) the surface tension *vs* the Fe content; (*d*) the viscosity *vs* the Fe content.

alloy is 0.06 pct and 0.67 pct larger than that of $Zr_{80}Fe_{20}$ and $Zr_{70}Fe_{30}$ alloys, respectively. In addition, the liquid density of $Zr_{9.8}Fe_{90.2}$ alloy is 0.54 pct less than that of $Zr_{16}Fe_{84}$ alloy and 1.52 pct higher than that of Fe at 1900 K. It is clear that the density gaps near these two eutectic compositions decrease with increasing temperatures. In addition, the density of the liquid Fe-rich Zr-Fe alloy is higher than the density of liquid iron, as measured by Lee *et al.*[42] This may be related to the evaporation of the sample, since the evaporation appears to be more severe with the Fe contents. On the other hand, the data extrapolated from the experimental results also cause the larger difference between the high Fe content alloys and pure iron at the same temperature.

The purple dotted line in Figure 5(a) displays the density change of the Zr-Fe alloys at the liquidus temperature. The trend of the density at the liquidus temperature $T_L$ is generally consistent with the trend of the density at other temperatures, except for two slight differences. The first difference is that the density of $Zr_{50}Fe_{50}$ alloy at its liquidus temperature is less than the density of $Zr_{60}Fe_{40}$ alloy. The second difference is that the density at the liquidus temperature of $Zr_{9.8}Fe_{90.2}$ alloy is larger than that of $Zr_{16}Fe_{84}$ alloy. These differences may be mainly caused by the differences in the liquidus temperature.

In general, it is difficult to obtain the density or other thermophysical properties of liquid alloys, especially for an undercooled liquid alloy. And hence, the Neumann–Kopp' law, which is based on the properties of pure elements, is used to estimate the properties of alloys when the data are unavailable, and high precision is not required. When the structure of a liquid alloy is close to an ideal solution, this approximation is feasible, and the data are useful. Because of the interatomic force, in the majority of cases, liquid alloys deviate from the ideal solution. To evaluate the deviation degree of this approximation for liquid Zr-Fe alloys, the excess volume *vs* Fe content in the temperature range of 1500 K to 1900 K is presented in Figure 5(b). The excess volume is given by the following expression:

$$\Delta V_E = V - V_0 = \frac{X_1M_1 + X_2M_2}{\rho} - \left(\frac{X_1M_1}{\rho_1} + \frac{X_2M_2}{\rho_2}\right), \quad [16]$$

where subscripts 1 and 2 refer to Zr and Fe, respectively, $V$ is the real volume, $V_0$ is the ideal volume, $\rho$ is the density of the alloys, and $X_i$, $M_i$, and $\rho_i$ are the atomic fraction, atomic weight and density of the components Zr and Fe, respectively. As shown in Figure 5(b), the Zr-Fe alloys all exhibit negative excess volumes in the temperature range of 1500 K to 1900 K, which may be related to the attractive interaction between Zr and Fe atoms. At 1500 K, the absolute value of the excess volume arrives at a maximum for $Zr_{16}Fe_{84}$ alloy, which means that $Zr_{16}Fe_{84}$ alloy may have the strongest atomic interaction, causing the maximum degree of the liquid alloy to deviate from an ideal solution. However, when the temperature rises to 1900 K, $Zr_{60}Fe_{40}$ alloy have the largest absolute value of the excess volume. As shown in Figure 5(b), the excess volume of $Zr_{16}Fe_{84}$ alloy changes the most in the temperature range of 1500 K to 1900 K. This may be related to the temperature coefficient of the density, since $Zr_{16}Fe_{84}$ alloy has the second largest temperature coefficient of the density, as shown in Table II. Among these compositions, $Zr_{70}Fe_{30}$ alloy has the lowest absolute value of the excess volume in the temperature range of 1500 K to1900 K, followed by $Zr_{9.8}Fe_{90.2}$ alloy. That means that the liquid $Zr_{70}Fe_{30}$ alloy is the closest to an ideal liquid. The purple dotted line in Figure 5(b), which shows the excess volume of Zr-Fe alloys at their own liquidus temperature, is consistent with the other constant temperature excess volume lines.

### C. *Surface Tension and Viscosity*

Both the surface tension and viscosity results of the liquid Zr-rich Zr-Fe alloys are measured by the drop oscillation method under electrostatic levitation conditions. The results of the surface tension are illustrated in Figures 6(a) through (e) and Table III. It can be seen that the surface tension of those five alloys all show a good linear dependence on temperature, which can be expressed as follows:

$$\sigma = \sigma_L + \frac{\partial \sigma}{\partial T}(T - T_L), \qquad [17]$$

where $\sigma_L$ is the surface tension at the liquidius temperature $T_L$, and $\partial\sigma/\partial T$ is the temperature coefficient. The surface tensions of the liquid Zr-Fe alloys all have the same tendency, increasing linearly with temperatures in both the undercooled and superheated states. At the liquidus temperature, the surface tensions for $Zr_{100-x}Fe_x$ alloys with $x$ = 10, 20, 24, 30, and 40 are 1.47, 1.54, 1.37, 1.33 and 1.59 N m$^{-1}$, respectively. Previously, Ohishi *et al.*[33] reports that the surface tension of the liquid $Zr_{76}Fe_{24}$ alloy at the liquidus temperature to be 1.44 N m$^{-1}$. Compared with the results obtained in this work, the difference is 5.11 pct. The main dissimilarity appears in the temperature coefficient, since the surface tension result measured by Ohishi *et al.* has a positive temperature coefficient which may be caused by impurities on the sample surfaces.

The temperature range and undercooling of the surface tension results of the Zr-Fe alloys are all listed in Table III. In the surface tension measurements, the temperature ranges of all Zr-Fe alloys except $Zr_{90}Fe_{10}$ have included both superheating and undercooling. For $Zr_{90}Fe_{10}$ alloy, the temperature range of the surface tension measurements is only below its liquidus temperature. The widths of the temperature range are different for different liquid Zr-Fe alloys, as a result of the difference in the liquidus temperature, the stability of the samples in levitation and so on. The surface tension of the liquid $Zr_{90}Fe_{10}$ alloy is measured in the narrowest temperature range of only 240 K, from 1743 K to 1983 K. In contrast, the surface tension of the liquid $Zr_{76}Fe_{24}$ alloy is obtained in the widest temperature range of 450 K, from 1123 K to 1573 K. Besides, by comparing Tables II with III, it can be seen that the undercooling values obtained in the surface tension measurements are generally lower than those obtained in the density measurements. For example, the maximum undercooling value that the liquid $Zr_{76}Fe_{24}$ alloy realizes in the surface measurements is 78 K, which is 64 K lower than the maximum undercooling value of 142 K obtained in the density measurements. The main reason is originated from the surface tension measurement method, which requires a liquid alloy drop to oscillate for gathering the drop oscillation frequency, and oscillation may limit the undercooling that liquid drop attained. Additionally, in contrast to the density measurements, where the sample is directly cooled down from a superheated temperature, the surface tension measurements need the sample to be maintained at different temperatures, which makes the metastable undercooled state vulnerable to be damaged.

Since the temperature ranges used to measure the surface tension of these five alloys are different, the same extrapolated process is employed. As shown in Figure 5(c), the surface tension of the liquid Zr-Fe alloys changes as the Fe content changes in the temperature range of 1300 K to 1800 K. The solid points are experimental results, and the hollow points are the data extrapolated from the experimental results. It can be seen that when the component Fe is light, the surface tension decreases slightly as the Fe content increases. Then, when the Fe content is larger than that of the eutectic composition $Zr_{76}Fe_{24}$, the values of the surface tension increase with increasing Fe contents in the temperature range of less than 1500 K.

The viscosity experimental results of the $Zr_{100-x}Fe_x$ ($x$ = 10, 20, 24, 30, 40) alloys are shown in Figures 6(f) through (j) and Table III. Since the decay time is derived from the decay curve, which also includes information on the characteristic oscillation frequency, the temperature range of viscosity is consistent with the surface tension data. The variation in the viscosity is expressed by an Arrhenius type equation as follows:

$$\eta = \eta_0 \exp\left(\frac{E}{RT}\right), \qquad [18]$$

where $\eta_0$ and $E$ are constant, and $R$ is the gas constant (8.314472 J mol$^{-1}$ K$^{-1}$). The results of the viscosity data fitted by Eq. [18] are displayed in Table III. The

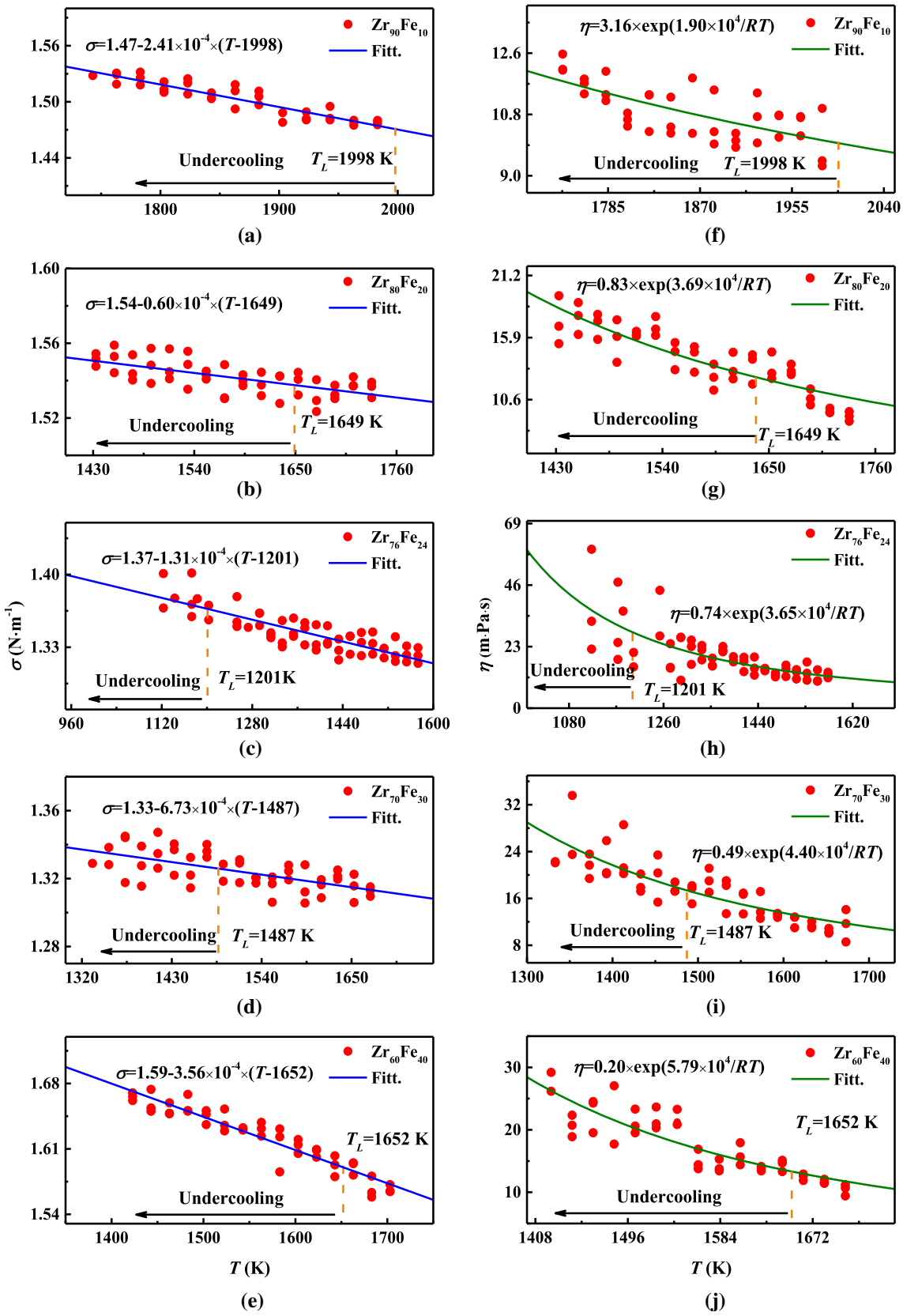


Fig. 6—The surface tension and viscosity of the liquid Zr-Fe alloys measured by the drop oscillation method: (*a* through *e*) the surface tension *vs* temperature; (*f* through *j*) the viscosity *vs* temperature.

**Table III. The Measured Surface Tension and Viscosity of the Liquid Zr-Fe Alloys**

| Alloy | $T_L$ (K) | Temperature Range (K) | Undercooling (K) | $\sigma_L$ (N m$^{-1}$) | Uncertainty of Surface Tension (Pct) | $\partial\sigma/\partial T$ ($10^{-4}$ N m$^{-1}$ K$^{-1}$) | $\eta_L$ (m Pa s) | Uncertainty of Viscosity (Pct) | $\eta_0$ (m Pa s) | $E$ ($10^4$ J mol$^{-1}$) |
|---|---|---|---|---|---|---|---|---|---|---|
| $Zr_{90}Fe_{10}$ | 1998 | 1743 to 1983 | 255 | 1.47 | ± 3.71 | − 2.41 | 9.92 | ± 5.82 | 3.16 | 1.90 |
| $Zr_{80}Fe_{20}$ | 1649 | 1433 to 1733 | 216 | 1.54 | ± 1.83 | − 0.60 | 12.15 | ± 4.56 | 0.83 | 3.69 |
| $Zr_{76}Fe_{24}$ | 1201 | 1123 to 1573 | 78 | 1.37 | ± 2.87 | − 1.31 | 28.62 | ± 19.45 | 0.74 | 3.65 |
| $Zr_{70}Fe_{30}$ | 1487 | 1333 to 1673 | 154 | 1.33 | ± 2.48 | − 6.73 | 17.21 | ± 3.13 | 0.49 | 4.40 |
| $Zr_{60}Fe_{40}$ | 1652 | 1423 to 1703 | 229 | 1.59 | ± 1.81 | − 3.56 | 13.54 | ± 2.74 | 0.20 | 5.79 |

viscosities of the $Zr_{100-x}Fe_x$ alloys with $x$ = 10, 20, 24, 30, and 40 at their respective liquidus temperatures are 9.92, 12.15, 28.62, 17.21, and 13.54 m Pa s, respectively. Compared with the liquid $Zr_{76}Fe_{24}$ alloy viscosity value of 47.33 m Pa s obtained by Ohishi *et al*. at the liquidus temperature, the difference is 65.37 pct. That difference is reduced to 36.16 pct at the temperature of 1473 K. This dissimilarity is caused by several factors. The temperatures of viscosity data measured by Ohishi *et al*. are all above the liquidus temperature of 1201 K, which may lead to a large data deviation under the liquidus temperature. Furthermore, the weaker undercoolability of $Zr_{76}Fe_{24}$ alloy compared to the other compositions also makes a larger data deviation for the undercooled liquid $Zr_{76}Fe_{24}$ alloy, which can be seen in Figure 6(h). From Table III, it can be seen that the $\eta_0$ of $Zr_{90}Fe_{10}$ alloy is an order of magnitude larger than that of the other alloys, which may be caused by the narrow temperature range that liquid $Zr_{90}Fe_{10}$ alloy obtained in the viscosity measurement.

The viscosities of the liquid Zr-Fe alloys *vs* the Fe content in the temperature range of 1300 K to 1800 K are shown in Figure 5(d). It can be seen that at the same temperature, the viscosities of the liquid Zr-Fe alloys tend to increase with increasing Fe contents, except for the decrease observed at $Zr_{76}Fe_{24}$ alloy. In addition, the viscosity of the liquid $Zr_{50}Fe_{50}$ alloy varies the most in the temperature range of 1300 K to 1800 K.

### D. *Measurements Uncertainty*

Since the experiments are carried out in a vacuum, volatilization is inevitable. The volatilization quantity depends on both the characteristics of the sample and the experimental conditions, such as the liquidus temperature of the sample and laser heating time. Therefore, the mass error is different for different compositions. Thus, here we consider $Zr_{76}Fe_{24}$ alloy as an example to illustrate the uncertainty in the measurements of these thermophysical properties.

In Eq. [2], which is used to measure the ratio between the specific heat and emissivity, the uncertainty is mainly caused by the error of the mass, surface area, cooling rate and temperature. The uncertainties of the mass, surface area and cooling rate are ± 0.03 pct, ± 0.10 pct and ± 0.50 pct, respectively. The uncertainty delivered from temperature is evaluated to be ± 2.00 pct. Then, the uncertainty in the measurement of $\xi$ for the liquid $Zr_{76}Fe_{24}$ alloy at the liquidus temperature is estimated to be approximately ± 2.11 pct. The uncertainties of the $\xi$ value obtained for the other Zr-Fe alloys at the liquidus temperature are all listed in Table I.

The uncertainty of the density measurement is mainly caused by the measurement error of the mass $\Delta m$, volume $\Delta V$, and temperature $\Delta T_{\text{err}}$. Therefore, the uncertainty of the density can be derived from the following expression:[35]

$$\frac{\Delta\rho}{\rho} = \sqrt{\left(\frac{\Delta m}{m}\right)^2 + \left(\frac{\Delta V}{V}\right)^2 + \left(\frac{\Delta T_{\text{err}}}{T}\right)^2}. \qquad [19]$$

The mass error is evaluated to be ± 0.03 pct from the difference between the mass of 32.65 mg before the experiment and 32.64 mg after the experiment. The uncertainty in the volume is mostly owing to the calibration factor and the random error of volume. Through calibration by a steel ball with a certain density, the relative uncertainty of the calibration factor is determined to be ± 0.43 pct. The other random error of ± 0.14 pct is obtained by calculating the volume at the same temperature. The uncertainty of the volume measurement is ± 0.45 pct. The relative uncertainty of the temperature is evaluated to be ± 0.50 pct. Finally, based on the abovementioned data and Eq. [19], the uncertainty of the density measurements made for the liquid $Zr_{76}Fe_{24}$ alloy at its liquid temperature is approximately ± 0.67 pct. The uncertainty of the density of the other Zr-Fe alloys is shown in Table II, which are all no more than ± 1.5 pct.

According to Eq. [4], the uncertainty of the surface tension $\sigma$ is mainly caused by the error in the characteristic frequency, density and radius measurements. For $Zr_{76}Fe_{24}$ alloy, the uncertainty delivered from the sample radius is about ± 2.31 pct. The uncertainty of the density is ± 0.67 pct, as described earlier. The uncertainty of the characteristic frequency is caused by rotation and the FFT analysis. The uncertainty caused by sample rotation is ± 1.41 pct, as estimated from the aspect ratio of the rotating liquid sample.[43] The uncertainty induced by the FFT analysis can be estimated to be approximately ± 0.70 pct, since the transformation error is less than 1 Hz, and the characteristic frequency is 142.33 Hz. Then, the uncertainty in the surface tension measurements made for the liquid $Zr_{76}Fe_{24}$ alloy at its liquidus temperature is estimated to be approximately ± 2.87 pct.

From Eq. [10], the uncertainty in the viscosity measurements can be approximately estimated from the error of the density, radius, and decay time. The uncertainties delivered from density and radius are ± 0.67 and ± 1.55 pct, respectively. The uncertainty in the decay time is determined to be approximately ± 19.38 pct. Thus, the uncertainty in the viscosity measurements made for the liquid $Zr_{76}Fe_{24}$ alloy at its liquidus temperature is ± 19.46 pct. The uncertainties in the surface tension and viscosity of the other compositions at the liquidus temperature are all listed in Table III.

## IV. CONCLUSION

The thermophysical properties of liquid Zr-Fe alloys have been measured by an electrostatic levitation technique, in both superheated and undercooled states. Under containerless and high-vacuum conditions, the electrostatically levitated Zr-Fe alloy drop is cooled by natural radiation, which allows for the measurements of the ratio of the specific heat to emissivity. Moreover, due to the low volatilization and single recalescence phenomenon, the hypercooling of 306 K for the undercooled liquid $Zr_{76}Fe_{24}$ alloy is obtained by combining an ideal insulation treatment with the single recalescence process. Then, the temperature-averaged constant pressure specific heat of the undercooled liquid $Zr_{76}Fe_{24}$ alloy is estimated to be 34.16 J $mol^{-1}$ $K^{-1}$. In addition, the hemispherical total emissivity of the undercooled liquid $Zr_{76}Fe_{24}$ alloy, which is derived from the ratio of the specific heat to emissivity, is linearly related to the temperature and is estimated to be 0.194 at its liquidus temperature. The densities of the liquid $Zr_{100-x}Fe_x$ alloys with $x$ = 10, 20, 24, 30, 40, 50, 84, and 90.2 all linearly decrease with the increasing temperature in both the superheated and undercooled states. Meanwhile, the absolute values of the density temperature coefficient of these Zr-Fe alloys show an increasing tendency with increasing Fe contents, which reveals that the liquid density sensitivity dependence on temperature increases with increasing Fe contents. The liquid density of the Zr-Fe alloys increasing with Fe contents at the same temperature represents a general trend, but there are two tiny drops near the two eutectic compositions of $Zr_{76}Fe_{24}$ and $Zr_{9.8}Fe_{90.2}$. The density gaps near these two eutectic compositions decrease with the increase in temperature. The surface tension and viscosity of the liquid $Zr_{100-x}Fe_x$ ($x$ = 10, 20, 24, 30, 40) alloys have been obtained by the drop oscillation method coupled with electrostatic levitation. Additionally, the surface tension experimental results show a linear dependence on temperature in the both superheated and undercooled states. The experimental viscosity data of the liquid Zr-rich Zr-Fe alloys have been described by an Arrhenius type equation. The uncertainties in the measurements of these thermophysical properties have been estimated at the liquidus temperature.

## ACKNOWLEDGMENTS

This work was financially supported by National Natural Science Foundation of China (Grant Nos. 51734008, 51327901), National Key R&D Program of China (Grant No. 2018YFB2001800), Shannxi Key Industry Chain Program (Grant No. 2019ZDLGY05-10) and Innovation Leadership Program in Sciences and Technologies for Young and Middle-aged Scientists. The authors are grateful to Dr. S.J. Yang, Mr. Q. Wang and Miss L. Wang for their help with the experiments.

## REFERENCES

1. Y.J. Lü and M. Chen: *Int. J. Mol. Sci.*, 2011, vol. 12, pp. 278–16.
2. S.H. Oh, M.F. Chisholm, Y. Kauffmann, W.D. Kaplan, W. Luo, M. Ruehle, and C. Scheu: *Science*, 2010, vol. 330, pp. 489–93.
3. M.P. Brenner and D. Lohse: *Phys. Rev. Lett.*, 2008, vol. 101, art. no. 214505.
4. B. Ribic, R. Rai, and T. DebRoy: *Sci. Technol. Weld. Joining*, 2008, vol. 13, pp. 683–93.
5. S.I. Sohn: *Phys. Rev. E*, 2009, vol. 80, art. no. 55302.
6. H.P. Wang, S.J. Yang, L. Hu, and B. Wei: *Chem. Phys. Lett.*, 2016, vol. 653, pp. 112–16.
7. L. Hu, L.H. Li, S.J. Yang, and B. Wei: *Chem. Phys. Lett.*, 2015, vol. 621, pp. 91–95.

8. B.O. Mukhamedov, I. Saenko, A.V. Ponomareva, M.J. Kriegel, A. Chugreev, A. Udovsky, O. Fabrichnaya, and I.A. Abrikosov: *Intermetallics*, 2019, vol. 109, pp. 189–96.
9. J.C. Bendert, M.E. Blodgett, A.K. Gangopadhyay, and K.F. Kelton: *Appl. Phys. Lett.*, 2013, vol. 102, art. no. 211913.
10. I. Saenko, A. Kuprava, A. Udovsky, and O. Fabrichnaya: *Calphad*, 2019, vol. 66, art. no. 101625.
11. J.D. Paulsen, J.C. Burton, and S.R. Nagel: *Phys. Rev. Lett.*, 2011, vol. 106, art. no. 114501.
12. E. de Miguel, N.G. Almarza, and G. Jackson: *J. Chem. Phys.*, 2007, vol. 127, art. no. 34707.
13. S. Jeon, D. Kang, S.H. Kang, S.E. Kang, J.T. Okada, T. Ishikawa, S. Lee, and G.W. Lee: *ISIJ Int.*, 2016, vol. 56, pp. 719–22.
14. T. Ishikawa and P. Paradis: *Crystals*, 2017, vol. 7, art. no. 309.
15. D. Kang, S. Jeon, H. Yoo, T. Ishikawa, J.T. Okada, P. Paradis, and G.W. Lee: *Cryst. Growth Des.*, 2014, vol. 14, pp. 1103–19.
16. H.P. Wang, B.C. Luo, and B. Wei: *Phys. Rev. E*, 2008, vol. 78, art. no. 41204.
17. P.C. Zhang, J. Chang, and H.P. Wang: *Metall. Mater. Trans. B*, 2020, vol. 51B, pp. 327–37.
18. W.J. Xie, C.D. Cao, Y.J. Lü, and B. Wei: *Phys. Rev. E*, 2002, vol. 66, art. no. 61601.
19. H.P. Wang, P. Lü, X. Cai, B. Zhai, J.F. Zhao, and B. Wei: *Mater. Sci. Eng. A*, 2020, vol. 772, art. no. 138660.
20. H.P. Wang, M.X. Li, P.F. Zou, X. Cai, L. Hu, and B. Wei: *Phys. Rev. E*, 2018, vol. 98, art. no. 63106.
21. K. Zhou and B. Wei: *Appl. Phys. A*, 2016, vol. 122, art. no. 248.
22. R.K. Wunderlich, H. Fecht, and G. Lohöfer: *Metall. Mater. Trans. B*, 2017, vol. 48B, pp. 237–46.
23. H.P. Wang, C.H. Zheng, P.F. Zou, S.J. Yang, L. Hu, and B. Wei: *J. Mater. Sci. Technol.*, 2018, vol. 34, pp. 436–39.
24. Q.L. Chu, M. Zhang, J.H. Li, F.X. Yan, and C. Yan: *Mater. Lett.*, 2018, vol. 231, pp. 134–36.
25. J.L. Lin, W.C. Zhong, Z.W. Cheng, H.Z. Bilheux, and B.J. Heuser: *J. Nucl. Mater.*, 2017, vol. 496, pp. 129–39.
26. W. Li, Y.Z. Yang, J. Xu, and C.X. Xie: *J. Alloy. Compd.*, 2017, vol. 710, pp. 644–49.
27. Q. Peng, E. Gartner, J.T. Busby, A.T. Motta, and G.S. Was: *Corrosion*, 2007, vol. 63, pp. 577–90.
28. A. Couet, A.T. Motta, and R.J. Comstock: *J. Nucl. Mater.*, 2014, vol. 451, pp. 1–13.
29. S. Martin, S. Richter, S. Decker, U. Martin, L. Krüger, and D. Rafaja: *Steel Res. Int.*, 2011, vol. 82, pp. 1133–40.
30. Y.X. Geng, Z.J. Zhang, Z.R. Wang, Y.M. Wang, J.B. Qiang, C. Dong, H.B. Wang, O. Tegus, and J. Non-Cryst: *Solids*, 2016, vol. 450, pp. 1–5.
31. L.T. Zhang, Y.P. Zhang, Y.K. Zhou, W.X. Tian, S.Z. Qiu, and G.H. Su: *Prog. Nucl. Energ.*, 2015, vol. 79, pp. 167–81.
32. T. Okawa and T. Nakajima: *Ann. Nucl. Energy*, 2017, vol. 101, pp. 182–95.
33. Y. Ohishi, H. Muta, K. Kurosaki, J.T. Okada, T. Ishikawa, Y. Watanabe, and S. Yamanaka: *J. Nucl. Sci. Technol.*, 2016, vol. 53, pp. 1943–50.
34. F. Stein, G. Sauthoff, and M. Palm: *J. Phase Equilib.*, 2002, vol. 23, pp. 480–94.
35. P.F. Zou, H.P. Wang, S.J. Yang, L. Hu, and B. Wei: *Metall. Mater. Trans. A*, 2018, vol. 49A, pp. 5488–96.
36. P.F. Zou, H.P. Wang, S.J. Yang, L. Hu, and B. Wei: *Chem. Phys. Lett.*, 2017, vol. 681, pp. 101–4.
37. A.J. Rulison and W.K. Rhim: *Rev. Sci. Instrum.*, 1994, vol. 65, pp. 695–700.
38. Y.S. Sung, H. Takeya, and K. Togano: *J. Appl. Phys.*, 2002, vol. 92, pp. 6531–36.
39. L. Rayleigh: *Proc. R. Soc. Lond.*, 1879, vol. 29, pp. 71–97.
40. K.V. Beard and J.Q. Feng: *Proc. R. Soc. A*, 1990, vol. 430, pp. 133–50.
41. P.F. Paradis, T. Ishikawa, G.W. Lee, D. Holland Moritz, J. Brillo, W.K. Rhim, and J.T. Okada: *Mater. Sci. Eng. R*, 2014, vol. 76, pp. 1–53.
42. J. Lee, J.E. Rodriguez, R.W. Hyers, and D.M. Matson: *Metall. Mater. Trans. B*, 2015, vol. 46B, pp. 2470–75.
43. P.F. Paradis and W.K. Rhim: *J. Chem. Thermodyn.*, 2000, vol. 32, pp. 123–33.